Available online at www.sciencedirect.com

ScienceDirect

Advances in Space Research 72 (2023) 2362–2376

ADVANCES IN SPACE RESEARCH (a COSPAR publication)

www.elsevier.com/locate/asr

# Measurement of electron fluxes in a Low Earth Orbit with SATRAM and comparison to EPT data

Stefan Gohl [a,b,*], Benedikt Bergmann [a], Martin Kaplan [a], František Němec [b]

[a] Institute of Experimental and Applied Physics, Czech Technical University in Prague, 11000 Prague, Czech Republic
[b] Faculty of Mathematics and Physics, Charles University, 18000 Prague, Czech Republic

Received 7 December 2022; received in revised form 16 May 2023; accepted 18 May 2023
Available online 24 May 2023

**Abstract**

We present the determination of electron fluxes measured by the Space Application of Timepix Radiation Monitor (SATRAM), a pixelated single-layer particle detector and the comparison with the Energetic Particle Telescope (EPT), a science-class radiation spectrometer. Both are attached to the Proba-V satellite of the European Space Agency. SATRAM hosts a Timepix chip with a 300 $\mu$m thick silicon sensor divided into a 256 × 256 pixel matrix with 55 $\mu$m pixel pitch. Simulations were conducted to determine the geometric factor of the sensor and the effective area that includes the shielding effects from all directions. The simulation was further used to study the influence of secondary particle production, track interruption, and backscattering on the number of detected particles. Particle identification is performed using two different methods. The first method requires that particle tracks are individually identifiable. A neural network was developed for this purpose, achieving an accuracy of 90.2% for particle identification. If individual particle tracks could not be identified, a statistical approach was used utilizing the energy deposition, average cluster energy, and the last known fraction of electrons. A comparison of the two instruments shows good agreement within one order of magnitude for the majority of the data.


*Keywords:* Cross calibration; Space radiation environment; Radiation monitoring; Particle tracking detector

## 1. Introduction

Earth is surrounded by a dynamically ever-changing radiation environment. The impinging solar wind causes disturbances inside Earth's magnetosphere, known as geomagnetic storms (e.g.Turner et al. (2019, 1994)) through magnetic reconnection (Dungey, 1961; Sugiura, 1964). These events cause increased particle fluxes in the radiation belts (Baker et al., 1997; Pandya et al., 2019; Zhao et al., 2019) and an increased ring current encircling Earth (Fok et al., 2001; Jordanova et al., 1997). The increased radiation during those event is a serious threat to astronauts (Cao, 2022) and satellite electronics alike (Tripathi, 2011; Adams et al., 2012). Even on Earth, this can have serious impact on communication, navigation, and power grids (Boteler et al., 1998; Kappenman, 1999; Kikuchi, 2003).

The nature of those solar wind – Earth magnetosphere interactions and the underlying mechanisms involved in these processes have yet to be fully understood. Efforts are being made to predict the geoeffectiveness of these storms, i.e., what solar parameters result in significant storms, as well as attempts to protect astronauts and equipment sent to space. To study these phenomena, more sophisticated detectors are needed. At the same time, these detectors should be small, lightweight, low maintenance,

* Corresponding author at: Institute of Experimental and Applied Physics, Czech Technical University in Prague, 11000 Prague, Czech Republic.
*E-mail addresses:* Stefan.Gohl@utef.cvut.cz (S. Gohl), Benedikt.Bergmann@utef.cvut.cz (B. Bergmann), frantisek.nemec@mff.cuni.cz (F. Němec).

https://doi.org/10.1016/j.asr.2023.05.033
0273-1177/

and ideally provide on-board processing capability. Large, complex detectors are rather difficult to deploy and sustain in space.

Two potential candidates are currently on board the Proba-V satellite of the European Space Agency (ESA) (Francois et al., 2014; Pro) launched in May, 2013. The satellite was brought into a Sun-synchronous Low Earth Orbit (LEO) with an altitude of 820 km at an inclination of 98.7°. The local time at descending node is between 10:30 a.m. and 11:30 a.m. and one orbit takes 101.21 min. The two instruments are the Energetic Particle Telescope (EPT) (Cyamukungu et al., 2014; Pierrard et al., 2020) and the Space Application of Timepix Radiation Monitor (SATRAM) (Granja et al., 2016; Gohl et al., 2019). EPT is a science-class radiation spectrometer with on-board signal processing for particle identification and classification. SATRAM is the first Timepix detector to be deployed in open space (Llopart et al., 2007). The aim for SATRAM was to test its functionality and to study its dosimetric capabilities, along with its suitability as a particle detector for space science applications.

Detectors of the Timepix family (there are four versions by now) (Wong et al., 2020; Poikela et al., 2014) and their predecessors of the Medipix family (likewise four versions) (Ballabriga et al., 2020) are already used in a wide variety of disciplines. Applications include X-ray imaging (Žemlicka et al., 2009; Ballabriga et al., 2013; Tichy et al., 2008), medical imaging (Rosenfeld et al., 2020; Butler et al., 2008; Procz et al., 2019), measurements of radiation environments and luminosity in high energy physics such as ATLAS (Bergmann et al., 2016; Bergmann et al., 2019a) and MoEDAL (Bergmann et al., 2021), and as a personal dosimeter for astronauts on board the ISS (Stoffle et al., 2015; Kroupa et al., 2015). Two other successful missions were launched into space involving Timepix detectors. The first one was LUCID on the TechDemoSAT-1 operated from 2014 to 2017 in a LEO orbit (Furnell et al., 2019). It featured five Timepix detectors. The second satellite named VZLUSAT-1 was launched into space in June 2013 and it is still running at this time (Baca et al., 2018). Here, one Timepix device is part of an X-ray telescope. Later generations of the Timepix/Medipix family significantly improve the performance, e.g. by allowing the 3D reconstruction of tracks within the sensor (Bergmann et al., 2017; Bergmann et al., 2019b) or by significantly reducing the detector's dead time.

The main advantages of Timepix detectors over common radiation monitors for space applications, such as the Standard Radiation Environment Monitor (SREM) (Evans et al., 2008; Sandberg et al., 2011; Siegl et al., 2010) or ICARE (Boscher et al., 2011; Boscher et al., 2014; Maget et al., 2014) are their much smaller size, weight, and larger fields of view. The latest development, the Miniaturized Radiation Monitor (MIRAM) (Gohl et al., 2022), is as small as $80 \times 60 \times 30$ mm$^3$, with a weight of 150 g and a power consumption of only 1.2 W. It also features on-board data processing for particle identification. Methods of particle identification have been proposed (Holy et al., 2008; Gohl et al., 2019), but are in need of optimization. A recent study successfully achieved the categorization of proton energies in several energy bins using a specifically designed neural network (Ruffenach et al., 2021). However, such a technique does not exist for electrons.

Unlike SATRAM, EPT has been designed as a science-class instrument for measuring energetic charged particles in the near-Earth radiation environment. It was developed to reduce resources (mass, volume, power consumption), while still delivering the same results and data products as other science-class instruments. It is required to provide a high energy resolution, high accuracy in particle identification, and to cover a wide energy range. The aim is to study magnetospheric events such as Ring Current formation during geomagnetic storms (Daglis et al., 1999) or mechanisms that fill the radiation belt with energetic particles from solar events or high energy cosmic rays originating outside the solar system (Walt, 1996) and other phenomena.

The first aim of this paper is to determine electron fluxes measured by SATRAM and present new methodologies for particle identification that are also valuable for future Timepix devices and can be used for on-board processing of the measured data to reduce the amount of telemetry data in space missions. The second aim is to compare and cross-calibrate results with EPT. The capabilities of Timepix detectors shall be demonstrated and involvement of the detector in future space missions encouraged. Therefore, a brief technical description of both instruments is given in Sections 2 and 3. Section 4 details the calculation of the electron fluxes from the SATRAM data, followed by the comparison of those fluxes with the fluxes measured by EPT in Section 5. The results are then discussed in Section 6 and conclusions are drawn in Section 7.

## 2. SATRAM

The SATRAM module is housed in an aluminum alloy compartment with dimensions of $55.5 \times 62.1 \times 107.1$ mm$^3$, weight of 380 g, and power consumption of 2.5 W. SATRAM was fixed on the outside of the satellite, with the sensor pointing away from the satellite. The top panel has a thickness of 1 mm with a thinned area above the Timepix sensor with a thickness of 0.5 mm.

Timepix is a hybrid (semiconductor) pixel detector. It features a 300 μm thick silicon sensor with a sensitive area of $1.4 \times 1.4$ cm$^2$ consisting of $256 \times 256$ pixels of pitch size 55 μm. The threshold level is set globally to 8 keV for the entire pixel matrix. During a so-called THL equalization the adjustment bits in each pixel are set in order to provide a homogeneous threshold level across the set of individual pixels. Usually, the lowest usable threshold is defined as the THL value which is 10 standard deviations above the noise edge and is for Timepix around 3–5 keV. However, considering the harsh space radiation environment and to better

cope with thermal variation, an additional margin of 3 keV was added. Data acquisition with the Timepix detector works in the following way: The sensor is set active for a certain amount of time, where the ionizing radiation is collected, after which the sensor is read out. During the read out time, the sensor is inactive. The resulting image is an illustration of the collected data in a 2D grid of identical volumes. This image is called a "frame". The time the sensor is active is set by the user. In the case of SATRAM, this acquisition time for consecutive frames has been set to 20 s, 200 ms, and 2 ms. The different times were intended to account for the different flux-levels encountered in orbit. SATRAM's Timepix detector is operated in the so called Time-over-Threshold (ToT) mode. The ToT measures the time a signal spends above the threshold level. This time can be associated with the deposited energy of a particle in each pixel via energy calibration (Jakubek, 2011), so that the energy loss per pixel per frame is measured. The full technical and operational details of SATRAM are described in Granja et al. (2016).

Particles that travel through the sensors leave signals in a conglomerate of adjacent pixels called tracks or clusters. Depending on the particle type, impact angle, and energy, the tracks can have a variety of appearances. Although the features are not entirely unambiguous, they can be used to identify particle type and energies. Example frames are shown in Fig. 1 with an acquisition time of 200 ms. Fig. 1a was taken near the poles, where the outer Van Allen belt intersects with the satellite orbit. It features a lot of thin, curly tracks that are typical for electrons. In the polar region, mostly only electrons are expected. The frame in Fig. 1b was taken at the edge of the South Atlantic Anomaly (SAA). There are many thick, straight tracks with higher energy deposition visible, as typical for protons with energies below ≈100 MeV. Protons with higher energies have thinner tracks similar to electrons, but the tracks are usually straight. Fig. 1c shows a track of a heavy particle, which may originate outside the solar system. Several electrons can be seen emanating from the main track; these are secondary electrons created in the sensor. The group of electrons to the right of the large track may also be secondary electrons created elsewhere in the SATRAM module by this heavy particle. The pixels in the lower left corner in all frames showing exceptionally high energy deposition are malfunctioning and are not considered in the analysis (see Section 4.6).

## 3. EPT

The other particle instrument on board Proba-V is EPT, a charged particle spectrometer. It has a volume of $127.5 \times 162 \times 211.5\ mm^3$, a mass of 4.6 kg, and a power consumption of 5.6 W. It therefore requires more resources than SATRAM, but is comparable to common radiation monitors. It was designed to be smaller, lighter, and less power consuming than other science-class instruments. On-board signal-processing techniques for particle identification and classification are a focal point of its design.

EPT has a low energy section and a high energy section. The former operates like a classical ΔE–E telescope and measures low energy particles. Furthermore, it serves as particle discriminator and trigger for all particle detections. This part also defines the field of view angle of 52° for protons. The high energy section consists of a series of digital and absorber modules operating as a telescope, which measures the particle energies of high energy particles. EPT provides six energy bins for electrons, ten for protons and ten for helium. The lower limits of incident energies are 0.5 MeV, 9.5 MeV, and 38 MeV for electrons, protons and helium, respectively. Upper limits are set by the number and characteristics of the absorber modules. Detailed information can be found in Cyamukungu et al. (2014).

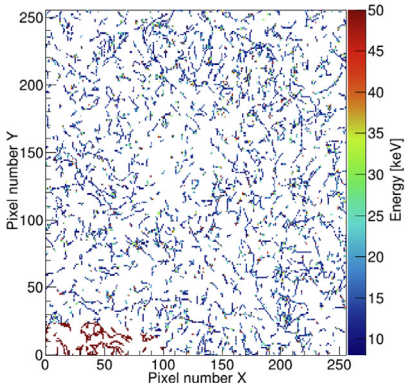


(a) Example frame with mostly electrons represented by thin, curly tracks. The frame was taken near the south pole on an ascending orbit~~poles~~[R2], where the outer Van Allen belt intersects with the satellites orbit.

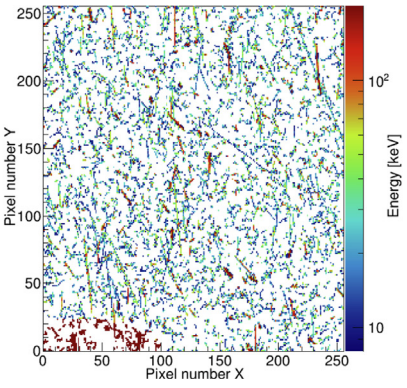


(b) Example frame taken at the edge of the South Atlantic Anomaly on a descending orbit[R2]. The thicker, straight tracks with higher energy deposition are protons with relatively low energy (< 100 MeV). Protons with higher energies have thinner, straight tracks.

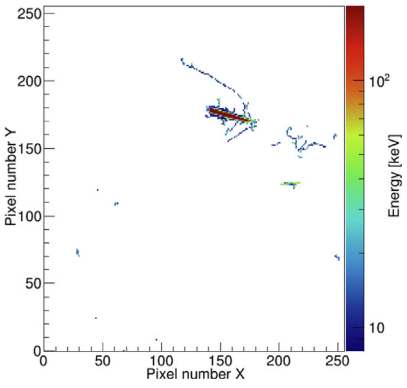


(c) Example frame with a heavy particle producing several secondary electrons, some of which are produced inside the sensor and some in the surrounding material. The frame was taken outside of any high flux area. The particles origin could be outside the solar system.

Fig. 1. Some example frames from different parts of the orbit with an acquisition time of 200 ms. Take note of the different color scales. Pixels in the lower left corner are malfunctioning and are not considered in the analysis.

## 4. Flux determination for SATRAM data

To determine the electron fluxes with Timepix in space, several aspects must be carefully considered. A set of simulations have been conducted to understand these aspects and to assist in the determination of the fluxes. A neural network (NN) was developed to identify the particle species based on track parameters. It is a complex algorithm using numerous features of the particle tracks in the pixel matrix of the Timepix detector. With increasing particle fluxes, chances are that tracks overlap, especially for cases of longer frames. Eventually, more and more tracks overlap each other, with single tracks no longer able to be identified and thus NN cannot be used any more. A different method will be used in these situations.

Another aspect is the geometry of the detector system. The sensor itself has a 4π field of view, but the surrounding material, such as the aluminum casing and the satellite itself attenuate or block the incoming radiation differently depending on the direction. Production of secondary particles or scattering may play a role. Furthermore, the sensor is a flat square shaped disk, but measures the radiation coming from all directions. Thus, the effective sensor area depends on the impact angle like $\cos(\theta)$.

To be able to directly compare the fluxes measured by the SATRAM and EPT instruments, it is vital to ensure that the fluxes were measured at the same time and locations. While both instruments are on the same satellite, they look in opposite directions, roughly perpendicular to the spacecraft orbit (approximately westwards and eastwards, respectively). Local or temporarily existing anisotropies might cause differences in the fluxes measured by the two instruments that are not related to the analysis itself. To bypass these issues, a time window of 60 s was chosen, in which the fluxes of both instruments were averaged over this time period.

EPT data was taken every two seconds and therefore, accounts for 30 data points in each 60 s window. SATRAM only provides one to four frames per time window. Each frame measured by SATRAM contains the complete pixel matrix of the Timepix detector. This is quite a lot of data, even after compression. The capacity of the telemetry is, however, considerably limited. Consequently, although the SATRAM measurements are continuous, only a fraction of the data is sent to Earth; the rest is lost. That also means that not all of the 60 s in the selected time window are covered by data. In the worst case, only 2 ms of SATRAM data might be available. Technically, this is also true for the EPT data. There might be less than 30 data points in the 60 s time window available. However, it happens significantly less than for SATRAM and for other reasons than limited telemetry. For the calculation of the average fluxes, the available acquisition time was used, not the 60 s. The time window serves purely as a selection criteria.

For each frame, the number of electrons $N_e$ was determined. Then, the total number of electrons in a given time window $N_e^{tw}$ was obtained (tw - time window). The electron flux $\Phi_e^{SATRAM}$ is then calculated as:

$$\Phi_e^{SATRAM} = \frac{N_e^{tw}}{A_e \; t \; g_f \; c_{sec} \; 4\pi} \tag{1}$$

with $A_e$ the effective area taking shielding effects of surrounding material into account; $t$ the total acquisition time of all frames in the time window; $g_f$ the geometrical factor defined as the relation between a spherical sensor and the actual flat sensor; $c_{sec}$ a correction factor for secondary production, track interruption and backscattering and 4π the general field of view of the Timepix sensor. The fluxes are calculated in units of particles per $cm^2 \cdot s \cdot sr$. What these factors indicate and how they were obtained is explained in the following sections.

### 4.1. Simulation

Simulations were performed using Geant4 (Agostinelli et al., 2003). All simulations use the same base code but with modifications in the particle source and the geometry of the model representing SATRAM and the satellite. This model is a simplified version of the actual SATRAM detector. Most of the electronics is excluded, but considering that their small size and their positioning between the sensor and the satellite, where the satellite is already providing a strong shielding, the impact of these components is negligible. The aluminum casing, the sensor and larger electronic components were included in the model.

A theoretical spectrum was used for the particle spectrum. This spectrum was created with the help of the SPENVIS online tool (SPE) using the AE-8-min model (Vette, 1991). Due to the casing thickness, low energy electrons are not able to penetrate the aluminum, cutting off the spectrum at a minimum energy of approximately 500 keV. Energies below this threshold are highly suppressed and therefore are considered immeasurable by SATRAM. The spectrum, together with the minimum energy marked by the red line, is shown in Fig. 2.

Simulations for protons were performed as well. They were done in the same manner with a spectrum from SPENVIS using the AP-8-min model (Sawyer and Vette, 1976). However, the radiation environment is dominated by electrons (by orders of magnitude), even low misclassification was found to have a strong impact on the proton flux rates determined with the method explained in Section 4.2.1. A more sophisticated measurement of proton fluxes thus requires improvements of current analysis techniques which is beyond the scope of the present analysis. Calculating proton fluxes will be done in future work together with heavier ions that are also present in the magnetosphere (Kovtyukh, 2020). Ion tracks are more similar to proton tracks and do not contribute to the error of the electron fluxes.

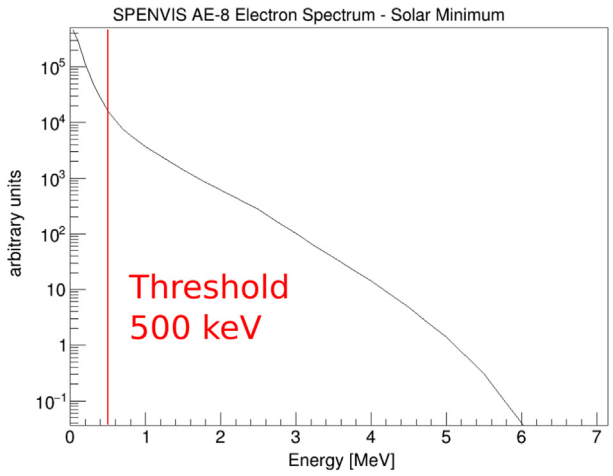


Fig. 2. Electron Spectrum acquired from SPENVIS online tool using the AE-8-min model. The red line at 500 keV marks the minimum energy of electrons that can reach the sensor in the SATRAM module.

### 4.2. Particle counting

Depending on the particle species, tracks can look very differently. Electrons often create curly tracks with a width of one pixel. Protons, on the other hand, create rather straight tracks with a thicknesses of several pixels depending on the energy. Particle identification was done via NN. For the network to work properly, single tracks must be recognized. However, for longer frame lengths and higher fluxes, the chance of two tracks overlap each other in the frame increases. They will be then recognized as one track. If the flux is high enough, the entire pixel matrix can be hit by an arbitrarily high number of particles and will be recognized as only one track. The occupancy was introduced to quantify the number of pixels that have been hit. It gives the fraction of hit pixels per frame related to the total number of pixels in percent. Frames with hit pixels of <20% were categorized as low occupancy frames; all others were categorized as high occupancy frames. The frames from Fig. 1a and 1c are low occupancy frames with occupancies of 14.2% and 0.8%, respectively. Fig. 1b is a high occupancy frame with an occupancy of 25.1%. For high occupancy frames, another method was applied. Both methods are explained in detail in the following sections.

#### 4.2.1. Low occupancy

The radiation measured by SATRAM mostly consists of electrons and protons with energies up to 7 MeV and 400 MeV, respectively. Therefore, the NN was developed to serve as a binary classifier for these two particle species. Heavier ions in the data are considered protons. The NN is a feedforward neural network created in the TensorFlow framework[1]. It was trained on simulated electron and proton data. Electron energies equally distributed to up to 7 MeV and proton energies equally distributed to up to 400 MeV were considered. The incoming flux was omnidirectional.

Seven features were used to classify a track: 1) the deposited energy, 2) the number of pixels, 3) the energy of the highest energy pixel, 4) the linearity of the track, 5) the roundness of the track, 6) the average number of neighboring pixels with an energy signal, and 7) the sum of absolute values of cubic and quadratic terms of a third order polynomial fit of the cluster. The architecture of the NN consists of an input layer, two hidden layers with seven neurons, and one output layer, as depicted in Fig. 3. A testing accuracy of 90.2% was achieved. The confusion matrix is shown in Fig. 4, which shows that the NN classifies 91% of the electrons as true electrons and 9% as protons, or false protons. For protons, 89% were true protons and 11% were false electrons. Thus, the number of measured electrons $N_e\prime$ and measured protons $N_p\prime$ can be written as:

$$N'_e = 0.91N_e + 0.11N_p \quad (2)$$

$$N'_p = 0.89N_p + 0.09N_e \quad (3)$$

where $N_e$ and $N_p$ are the true number of electrons and protons, respectively. This is a system of two linear equations and two unknowns $N_e$ and $N_p$. Solving this leads to:

$$N_e = \frac{89 \cdot N'_e - 11 \cdot N'_p}{80} \quad (4)$$

$$N_p = \frac{91 \cdot N'_p - 9 \cdot N'_e}{80} \quad (5)$$

These equations give the true number of electrons and protons according to the NN. However, when applying this method to the SATRAM data, the true number of protons is often close to zero or negative. Considering that the electron fluxes in the inner Van Allen belt are often approximately two orders of magnitude higher than the proton fluxes, it can be seen that the error of the electrons is the

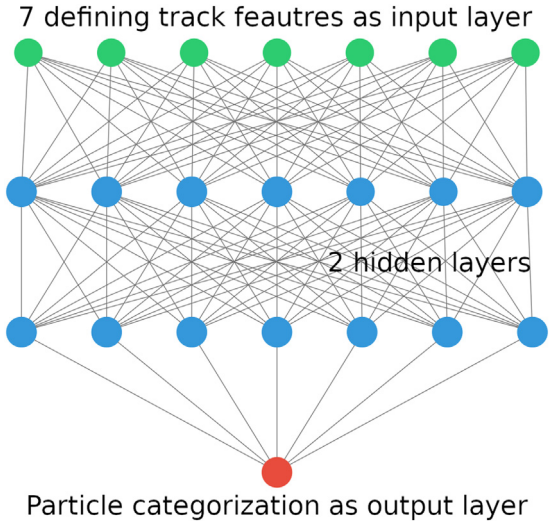


Fig. 3. Scheme of the neural network with one input layer with seven features, two hidden layers and one output layer.

[1] https://www.tensorflow.org/?hl=cs.

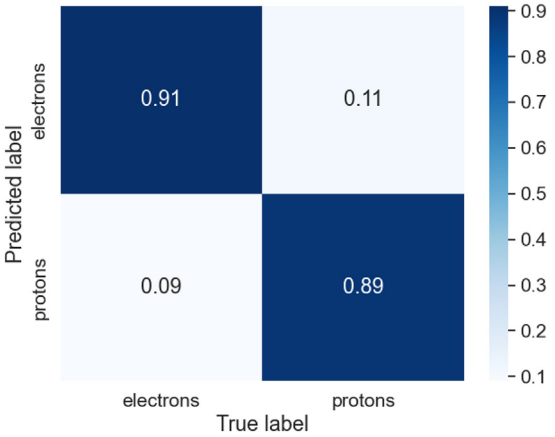


Fig. 4. Confusion matrix for the neural network between truly and falsely identified protons and electrons.

same order of magnitude as that of the proton fluxes. For this reason, proton fluxes cannot be derived using this method, and therefore they are not further considered in this work. Regarding the electrons, Eq. 4 was used to calculate $N_e$ in the case of low occupancy frames.

#### 4.2.2. High occupancy

In the case of high occupancy frames, the identification of single particles is impossible due to the increased number of overlapping tracks. Therefore, a different method was applied. For this, an estimate of the mean track energy as well as the fraction of electrons at each satellite position is needed. The former was obtained by using frames with low occupancy. For that, the world map was first divided into bins as seen in Fig. 5. The meta data of each frame contains the information about the longitude and latitude, where it was measured. In each bin, using only low occupancy frames, the average deposited energy of all tracks was calculated to estimate the local mean energy of all particles in the area.

The fraction of electrons was determined by using the last low occupancy frame measured before the current high occupancy frame. There, the fraction of electrons and protons was measured and is used for the high occupancy frame.

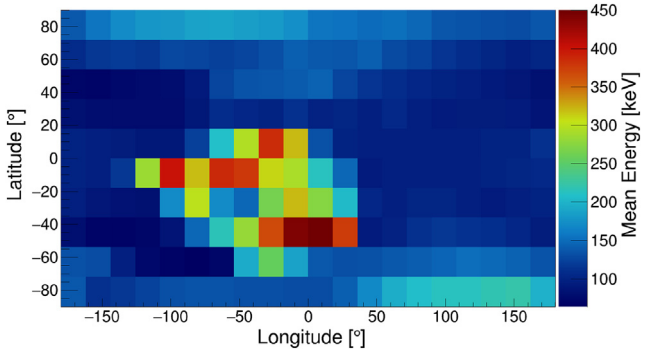


Fig. 5. Map of the local mean energy of particles measured with low occupancy frames from 2015 to 2019.

The number of electrons $N_e$ in high occupancy frames was then calculated according to:

$$N_e = \frac{E_{tot}}{E^{loc}_{mean}} \cdot \frac{N^{last}_e}{N^{last}_e + N^{last}_p} \tag{6}$$

with $E_{tot}$ the total energy of the full frame, $E^{loc}_{mean}$ the local mean energy according to the current satellite position in Fig. 5, $N^{last}_e$ and $N^{last}_p$ the number of electrons and protons, respectively, determined in the last low occupancy frame before the current frame.

### 4.3. Effective area

Another simulation was conducted to determine the influence of the material surrounding the sensor including the satellite. The setup was as described in Section 4.1 with a spherical particle source shooting electrons to the center of the sphere, where the center of the sensor is located. The energy spectrum of the electrons was above 500 keV as in Fig. 2. Four additional simulations were performed, where the center of the spherical source was moved, so it would fall onto each of the four corners of the sensor.

The number of electrons that reached the detector $N_{det}$ was then divided by the total number of simulated particles $N_{sim}$ and multiplied by the surface area of the detector $A_s$. This number is labeled the effective area $A_e$.

$$A_e = \frac{N_{det}}{N_{sim}} \cdot A_s = 0.19\ \text{mm}^2 \tag{7}$$

### 4.4. Geometric factor

To account for the shape of the sensor, two simulations were conducted from which the geometrical factor was then derived. The first simulation included only the bare sensor. The particle source was a sphere with a small radius, so the sensor would just fit inside. Electrons were emitted inwards at a random angle to create a truly omnidirectional flux. The number of particles that hit the detector $N_{sensor}$ were counted. In the second simulation, the sensor was replaced with a spherical sensor with the same surface area. The particle source was the same as before and the number of particles hitting the sphere $N_{sphere}$ were counted. The geometric factor was then calculated according to:

$$\frac{N_{sensor}}{N_{sphere}} = g_f = 1.11 \tag{8}$$

### 4.5. Secondary particles, track interruption and backscattering

The material surrounding the sensor is a potential source for secondary particles. Knock-out electrons,

Bremsstrahlung or photons emitted by excited atoms are possible candidates. Secondaries can also be produced within the sensor material. This was investigated in yet another simulation. The simulation setup was the same as in the last section. Then, three simulations were conducted with slightly different settings: 1) both primary and secondary particles were tracked; 2) only primary particles were tracked; and 3) only secondary particles were tracked. To ensure, that each simulation was creating the same events, the seeds for the simulation were set to specific values and not randomized like in other simulations in this work. The numbers were then compared to get a sense of the number of secondaries produced and consequently the number of additional particles counted which did not originate from the flux in space.

During this investigation, two additional effects appeared to be closely connected. Electrons can create interrupted tracks. Along the trajectory of an electron inside the sensor hitting several pixels, the deposited energy in one of the pixels in the middle of the track may be not high enough to reach the energy threshold of 8 keV and thus the pixel will not be triggered. In the frame, it will look like there are two tracks instead of one. In the analysis, it is impossible to distinguish if those tracks are originating from two events or one. The other effect is that an electron can leave the sensor and be scattered back into the sensor by the surrounding material. This particle then creates another track that is not distinguishable from a separate event.

A simulated event including backscattering, track interruption and the production of secondary particles probably within the sensor is displayed in Fig. 6. It consists of a long slightly curved track and a shorter track several pixels away from the larger track. In Fig. 6a, the whole event is shown. In the analysis of real events, this would be considered as two separate events. Fig. 6b shows the same event without secondary particles. The presence of both, the shorter and longer tracks, suggests that the primary particle was scattered somewhere outside the sensor and moved back to the sensor to create another track separate from the first. It can be also seen that the longer track is interrupted. There are two secondary particles shown in Fig. 6c. It is clear that the two secondaries are in the same area of the sensor as the primary particle and they are not evaluated as separate events. In fact, one of the secondaries even connects to the interrupted primary track, thus mitigating the issue of artificially creating a separate event.

Therefore, it seems that secondary particle production is not a large issue. Most secondaries in the data seem to be produced within the sensor material and are connected to the primary particle track, thus not increasing the particle count artificially. Secondaries even appear to mitigate the issue with interrupted tracks, though this does not always has to be the case. It can, of course, happen that a secondary particle created in the surrounding material finds its way into the sensor. In that case, the primary particle can also be scattered away from the sensor and only the secondary particle is measured. However, this seems to be rare. Even rarer is the case of primary and secondary

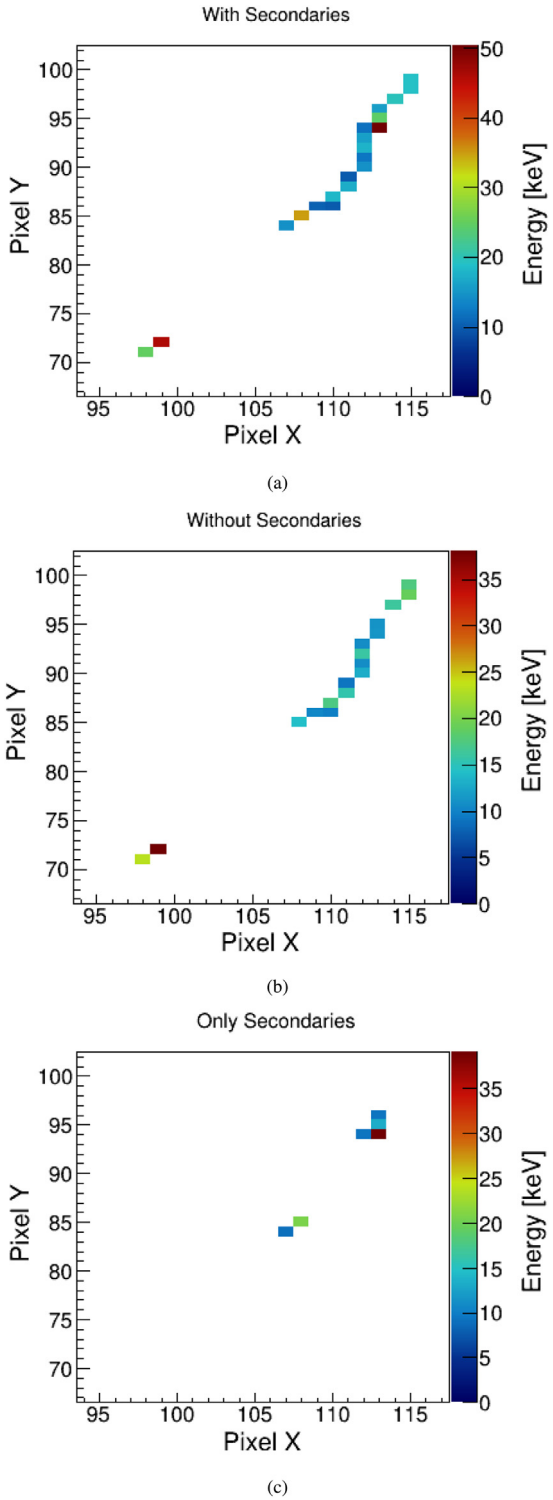


Fig. 6. Example of an interrupted electron track with a backscattered electron and two secondary particles. (a) The full event is displayed. (b) Only the primary track is presented, showing that the track is interrupted and a separate track is coming from the primary event, probably due to a particle backscattered into the sensor. (c) Only the secondary particles are shown. They do not create a separate particle track. However, because of the backscattering, this event would still be counted as two.

particles producing two separate events in the sensor. A larger issue is the interrupted tracks and the backscattered events. Fig. 7 shows a real data event with several interruptions in the particle track. This event could be an electron or a high energy proton. The perfect alignment suggests that it is a single event. However, theoretically, it could also be coincidence where there are three particles responsible. There is no guarantee for either case.

The number of events in the simulation with primary and secondary particles $N_{count}$ divided by the number of primary particles that reached the detector $N_{prime}$ give a correction factor for secondary production, track interruption and backscattering $c_{sec}$ combined:

$$\frac{N_{count}}{N_{prime}} = c_{sec} = 1.22 \tag{9}$$

### 4.6. A note on noisy pixels

Right after the start of the Proba-V mission, a few hundred or so pixels showed erroneous behavior. In one corner of SATRAM's sensor, the pixels always showed the maximum measurable amount of deposited energy in each pixel instead of the actual deposited energy. Those pixels are not considered in the analysis.

Pixels that trigger by themselves without being hit or those that show unusual high energy values are called noisy pixels, because of their electronic noise (Bergmann et al., 2020). This is a common issue in detectors of the Timepix family. When identified, those pixels are then masked, i.e., the signal they produce is not recorded. In some cases, resetting the pixel matrix can eliminate the issue, at least temporarily. An independent study - not presented in this work - has shown, that noisy pixels in SATRAM are scarce, apart from the aforementioned corner, and thus are not an issue for this study. This concerns the data produced until the end of 2019. A correction was, therefore, not considered.

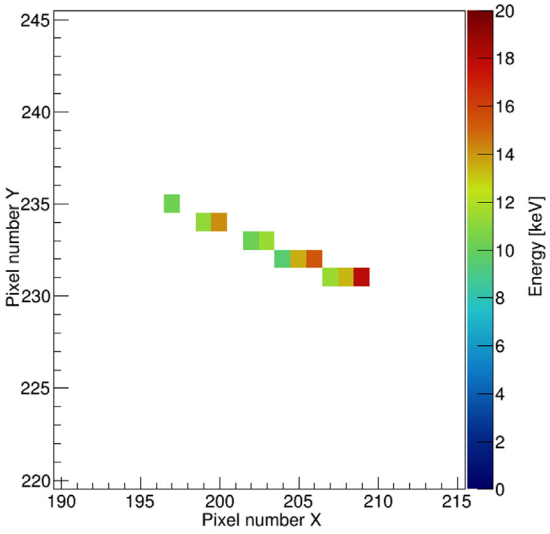


Fig. 7. A real event measured on November, 20th in 2014 at 12:50:30 UT, featuring an electron or minimum ionizing particle impact and a track interruption. This event is counted as three events in the data analysis, even though the perfect alignment suggests that this is a single event. The data can be viewed on: https://satram.utef.cvut.cz/.

## 5. Comparison with EPT

Having demonstrated the method of calculating electron fluxes from the SATRAM data, it can now be compared with the EPT measured fluxes. The EPT data can be retrieved from the ESA Space Weather Service Network via log-in[2]. Electron fluxes are provided as differential fluxes with a 2 s time resolution in six energy bins (500–600 keV, 600–700 keV, 700–800 keV, 800–1000 keV, 1000–2400 keV and 2400–8000 keV). SATRAM can only measure integral fluxes and there are no energy bins, because the energy of the electrons cannot be determined. Therefore, the EPT fluxes must be integrated over all energy bins for the comparison. Coincidently, the energy range of both instruments overlap perfectly and no further adjustments have to be made. Just as for the SATRAM data, average fluxes in the same 60 s time windows are calculated.

Fig. 8 shows the electron fluxes measured in the year 2015 as a function of time and L-shell. The results obtained by the EPT and SATRAM instruments are shown in the top and bottom panels, respectively. The L-shell values are provided by the EPT group and they are available in the online files. The EPT data appears a lot smoother than the SATRAM data. A possible reason for this is the limited amount of data that is send to Earth by the satellite. While the detector measures continuously without interruption, the amount of data that is produced is simply too much for the satellite to transmit to the ground station. Instead of cutting of the data after the transmission limit is reached, frames are not saved consecutively, but spread out so the whole orbit is still covered. This also means that the data available during the 60 s time window can be greatly reduced.

Another contributing factor can be the much larger active area of the EPT detector. While SATRAM has an effective area of 0.19 mm$^2$ (Eq. 7), EPT's entrance window has an area that is three orders of magnitude larger than that. Therefore, the sensitivity of EPT in terms of minimal quantity of registered particles is higher than the sensitivity of SATRAM. However, at high fluxes, where there are hundreds of thousand of particles per cm$^2$ per second, the size of the detector should not matter when measuring fluxes. So, the SATRAM data should be smoother at higher fluxes according to this. That is not the case. The comparatively small effective area of SATRAM may, however, contribute to the coarseness at low fluxes.

[2] https://swe.ssa.esa.int/csr-ept-federated.

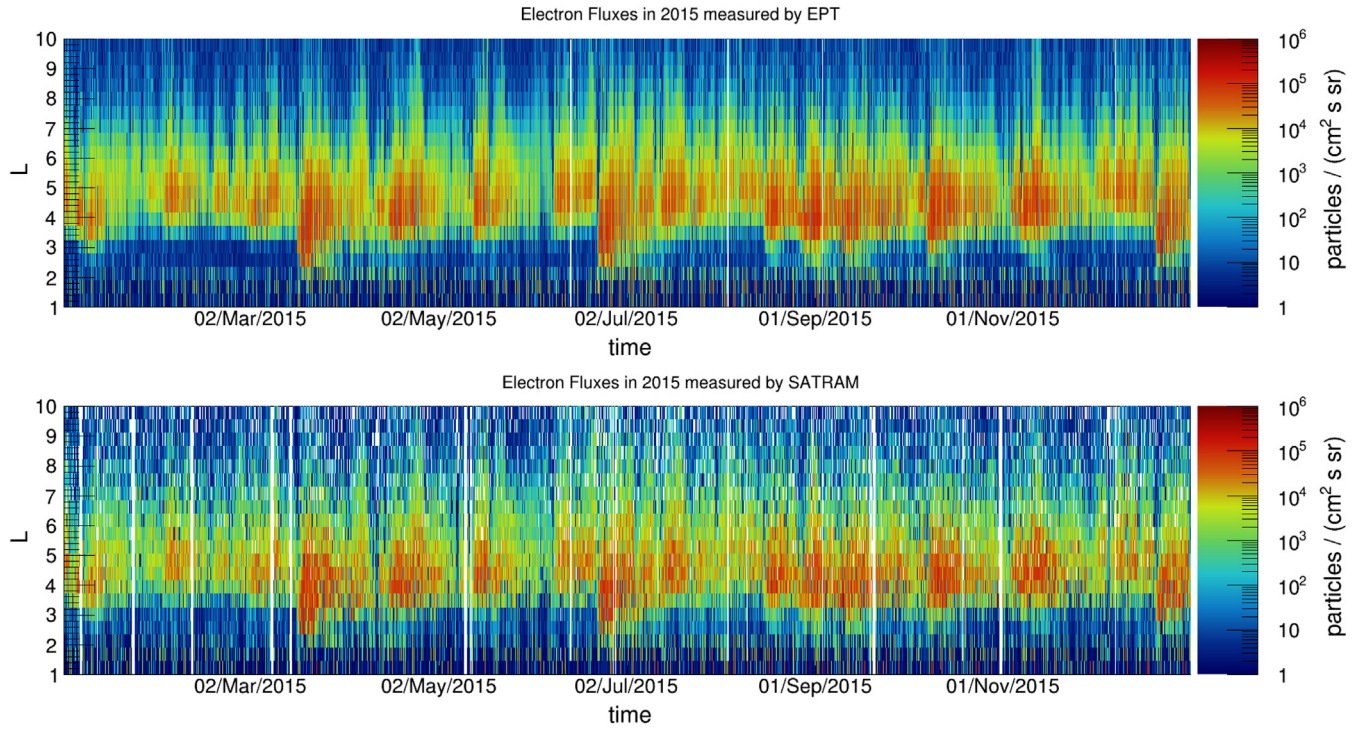


Fig. 8. Electron fluxes as a function of time (60 s bins) and L-shell (0.5 bins) for EPT (top) and SATRAM (bottom) for the year 2015. EPT data appear smoother than SATRAM. In terms of general flux variations, both instruments seem to agree.

Apart from the smoothness of the data, the results look very similar. Flux variations at certain L-shells appear in both plots at the same time. They seem to generally agree. Similar results are obtained for the following years (see Appendix A).

Another way to compare the data is by plotting the SATRAM fluxes on one axis of a 2D-histogram and the EPT fluxes on the other axis. This was done in Fig. 9a with the EPT fluxes on the x-axis and the SATRAM fluxes on the y-axis for the year 2015. Ideally, all results would be on the unity line, represented by the black diagonal line. The deviation from the line is not larger than one order of magnitude for the majority of data points. This is demonstrated by the magenta lines shown in the plot. There are only a few points further away. The correlation factor between the two data sets was determined to be

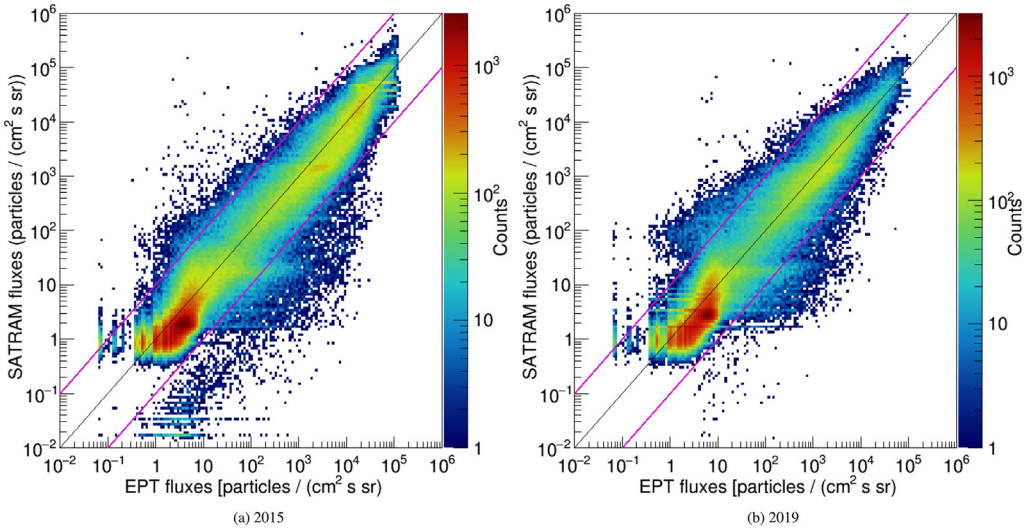


(a) 2015 (b) 2019

Fig. 9. The SATRAM fluxes are compared with the EPT fluxes in 2D-histograms for the years (a) 2015 and (b) 2019 with correlation factors of 0.83 and 0.85, respectively. The majority of data is concentrated close to the unity line. The magenta lines mark differences in fluxes of one order of magnitude.

0.83 for the year 2015. A large portion of the data can be seen at low fluxes (< 10 particles per $cm^2 \cdot s \cdot sr$) with SATRAM fluxes slightly smaller than EPT fluxes. A slight narrowing can be seen at around 50 particles per $cm^2 \cdot s \cdot sr$ on the y-axis showing the SATRAM fluxes. This is most likely a result of the two methods applied for the calculation of the fluxes. SATRAM fluxes above the narrowing are also slightly below EPT fluxes. For very high fluxes (> 10,000 particles per $cm^2 \cdot s \cdot sr$), this is no longer true and the two data sets are in large agreement. At the lower left end, some vertical and horizontal lines can be seen. These are most likely artifacts of the integration time of both instruments. Similar plots have also been prepared for other years. In Fig. 9b, the results for the year 2019 are presented. A correlation factor of 0.85 was determined. Little to no change to the overall result can be seen. The plots for other years are presented in Appendix A.

Furthermore, the distribution of the electron fluxes in terms of their satellite position around the globe was investigated. In Fig. 10, average fluxes measured by both instruments in the year 2015 were plotted according to the latitude and longitude of the respective satellite position. Both maps show very similar distribution. The highest fluxes are in the SAA in the center and in two bands near the poles, where the outer radiation belt intersects with the satellites orbit. The white area over Europe is where the satellite communicates with its ground station in Belgium and therefore no data is measured in this area.

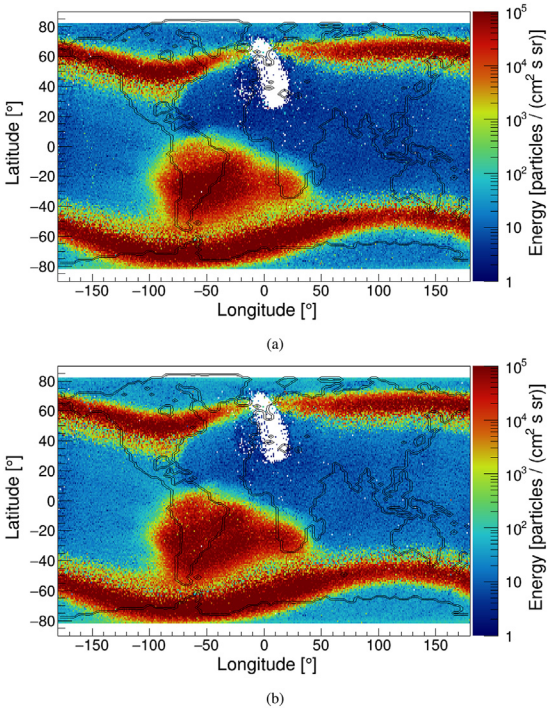


Fig. 10. Flux distribution over the world measured by (a) SATRAM and (b) EPT for the year 2015.

## 6. Discussion

For the most part, SATRAM and EPT data are in satisfactory agreement. In direct comparison, most data points are located near the unity line, as seen in Fig. 9. SATRAM fluxes are often slightly lower than EPT fluxes. Further, the majority of data points are spread over a range from approximately one order of magnitude above the unity line to about one order of magnitude below the unity line. The reasons for this can be manifold and it is generally not possible to deduct from such a plot which instrument measures the correct flux. Additionally, note that the instruments look in opposite directions at all times. This may be, along with an anisotropic electron distribution in the lower layers of the Earth's magnetosphere (Dudnik et al., 2022), a possible reason for part of the observed spread. In a recent work (Pierrard et al., 2021), electron fluxes from EPT at LEO were compared with data from the Van Allen Probes at medium Earth orbit (MEO). Although, these missions fly on different orbits, the conditions should be at least similar for the same L-shell at the same time. The Pierrard et al. paper demonstrates good agreement between the two datasets. This work demonstrates that SATRAM data can be trusted on a similar level.

The major issue concerning SATRAM data is the low coverage of the data over time. While EPT has up to 30 data points in a 60 s window SATRAM has only up to 5 points, even though the Timepix is measuring continuously. The problem here lies in the large amount of data that cannot be transmitted to Earth. However, this is an issue that can easily be avoided in future projects.

Additionally, it was observed that some frames were saturated. Particularly in the SAA in 20 s long frames, the detector can reach its limit. Saturation in the energy measurement has been found to underestimate the electron fluxes of up to a factor of five. This can be avoided by shortening the frame times, at least for specific regions.

Current developments address many of the issues SATRAM has. A new device was already developed and it is currently awaiting its launch into space (Gohl et al., 2022). It features a Timepix3 detector, the successor of Timepix, combined with on-board processing to determine the electron and proton fluxes. Thus, the amount of data that needs to be transmitted to Earth is greatly reduced. Further developments to allow the energy determination of electron energies are underway. This can be achieved by putting electron filters in front of the sensor. The differences in the measured intensity and energy deposition underneath these filters can then be used to assess the energy spectrum of the electron component in the radiation field in few bins. Another development is called Hardpix. It can feature one or two Timepix3 devices. Two Hardpix devices are planned for the Lunar Gateway mission, the station that is planned to circle the Moon. Although there are currently no such plans, interplanetary missions are another possibility for the future.

## 7. Conclusion

The Proba-V satellite hosts two particle instruments, the EPT and the SATRAM module. EPT is a technology demonstration that has the size and power consumption comparable to a common radiation monitor for space applications, but has the functionality of a science-class particle spectrometer. SATRAM is also a technology demonstrator, but with less ambitious goals originally. It does not have the spectroscopic capabilities of EPT, but its size and power consumption are significantly smaller. In this work, the electron fluxes seen by SATRAM have been determined and compared with the electron fluxes measured by the EPT instruments.

To identify particle species in the SATRAM data, a NN was developed. An overall accuracy of 90.2% was achieved, but it requires the ability to identify individual particle tracks. At higher fluxes, this becomes increasingly difficult, as overlapping tracks occur more and more frequently. Eventually, it becomes impossible to apply this method. An alternative method was thus introduced that uses the total deposited energy in the frame, divided by the local average energy and multiplied by the last known fraction of electrons in the frame. The accuracy of the neural network is insufficient to determine proton fluxes.

A multitude of Geant4 Monte-Carlo simulations have been conducted to determine geometric and other correction factors. The effective area takes accounts for the direction dependent shielding. The flat shaped sensor was compared to a spherical detector of the same surface area to specify a geometrical factor. Finally, a simulation was performed to study the effect of secondary radiation in the SATRAM device in combination with track interruption in the sensor and backscattering of particles that already left the sensor.

A comparison of the electron fluxes measured by SATRAM with the electron fluxes measured by EPT showed good agreement for most of the data. Differences in the fluxes are mostly below one order of magnitude. The discrepancy might be due to an insufficiently precise determination of the electron–proton content of the frames, a statistically low amount of data due to limitations of the data transmission of the satellite or saturation effects of the pixels. A saturation effect was observed with a deviation of a factor up to five.

Improvements could be achieved by a more complex pattern recognition software and an independent method to determine the electron–proton distribution for each frame. Technological advancements over the recent years allow for better performing devices and on-board processing without necessarily increasing the need for more resources (size, mass and power). This would solve one of SATRAM's major drawbacks and reduce the amount of data for transmission to Earth and, therefore, save the data of the continuous measurements. Another major issue of SATRAM is the lack of spectroscopic information. This can be solved by using a NN to recognize different proton energies from individual tracks (Ruffenach et al., 2021). Electron energies could be determined by mounting electron filters in front of the sensor. Its small size and relatively low power consumption provide an advantage of commonplace instruments for space radiation. It can also be integrated in more complex detector systems and function as a complement to existing technology.

## Declaration of Competing Interest

The authors declare that they have no known competing financial interests or personal relationships that could have appeared to influence the work reported in this paper.

## Acknowledgments

The authors acknowledge funding from the European Space Agency (Contract Number:4000122160/17/UK/ND) for the SATRAM project. Further acknowledgment goes to the Center for Space Radiations of the Université Catholique de Louvain (UCL/CSR) and The ESA Space Safety Programme for the EPT data. Special thanks go to Viviane Pierrard and Edith Botek for all the help regarding this study. The authors also acknowledge funding from the Czech Science Foundation (GACR) under Research Project No. 23-04869M. Additionally, the authors Stefan Gohl and František Němec acknowledge the support of GACR Grant 21-01813S.

## Appendix A. Complete Data

See Figs. A.11, A.12, A.13, A.14 and A.15.

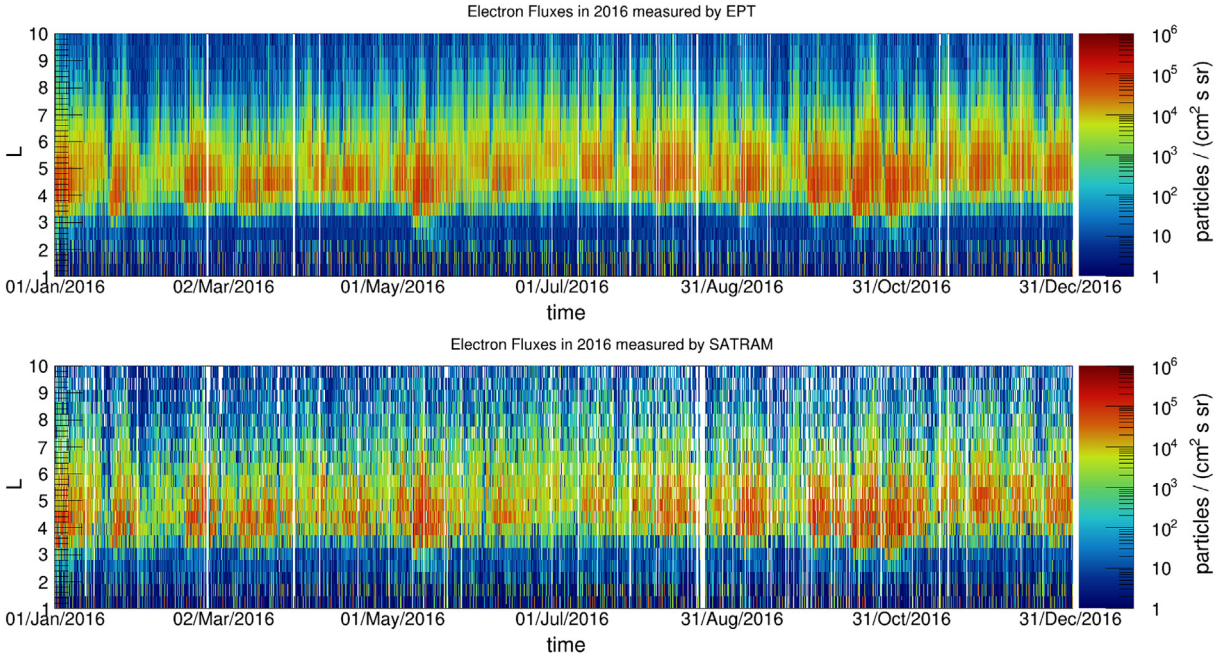


Fig. A.11. Electron fluxes as a function of time (60 s bins) and L-shell (0.5 bins) for EPT (top) and SATRAM (bottom) for the year 2016.

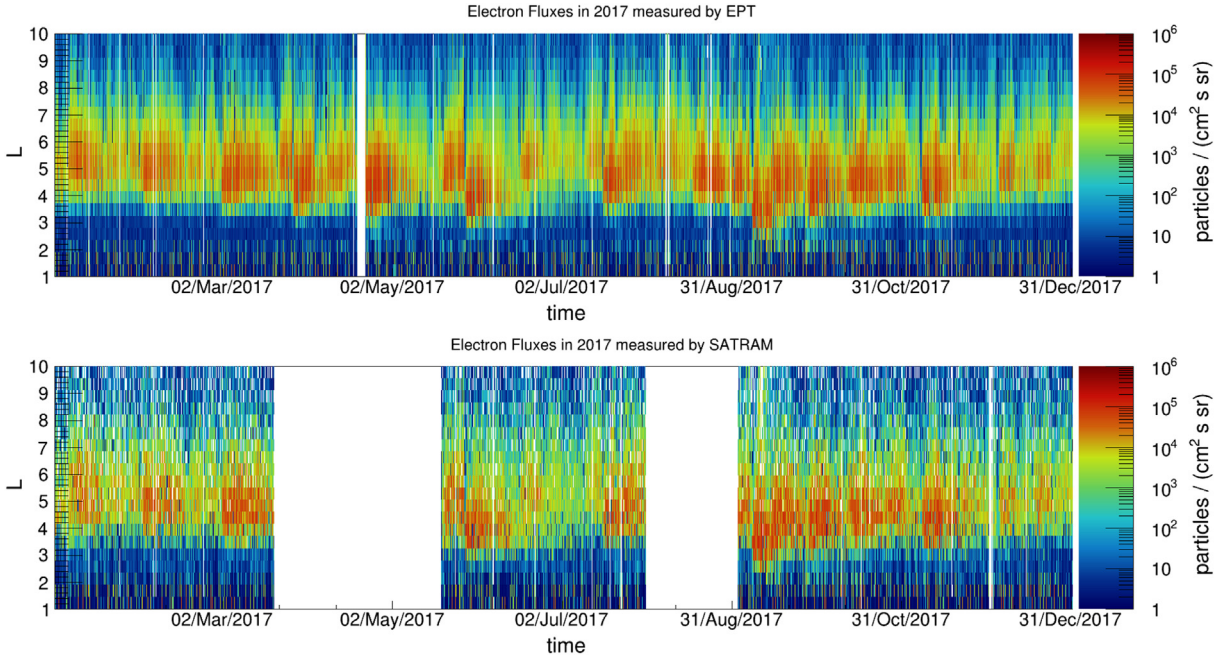


Fig. A.12. Electron fluxes as a function of time (60 s bins) and L-shell (0.5 bins) for EPT (top) and SATRAM (bottom) for the year 2017.

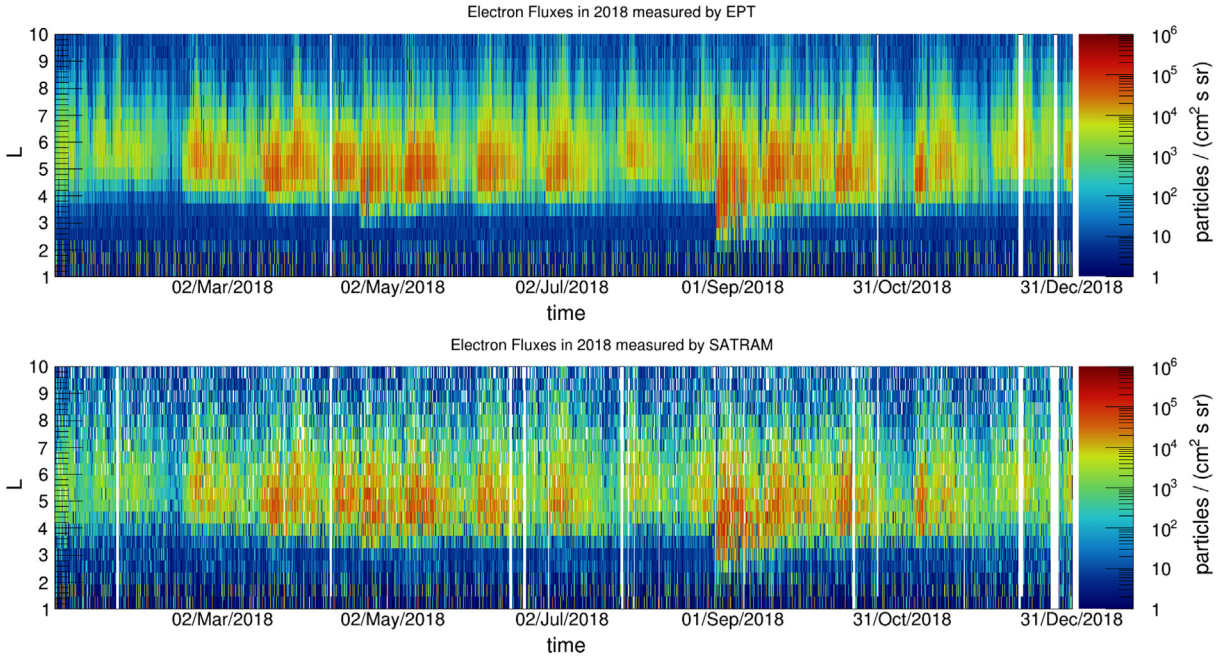


Fig. A.13. Electron fluxes as a function of time (60 s bins) and L-shell (0.5 bins) for EPT (top) and SATRAM (bottom) for the year 2018.

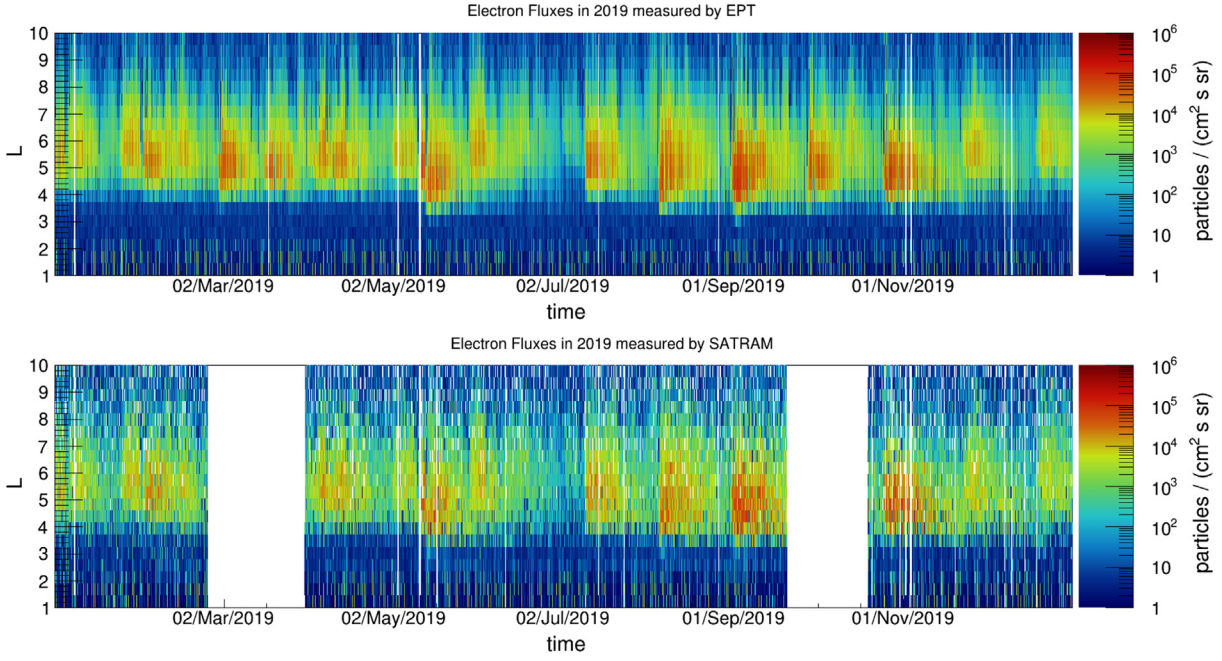


Fig. A.14. Electron fluxes as a function of time (60 s bins) and L-shell (0.5 bins) for EPT (top) and SATRAM (bottom) for the year 2019.

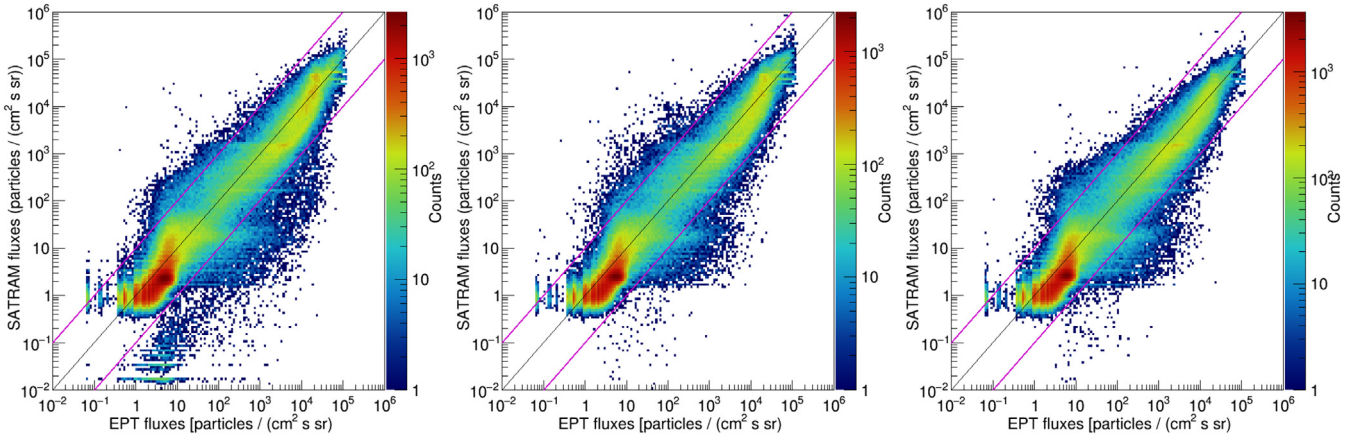


(a) 2016 (b) 2017 (c) 2018

Fig. A.15. The SATRAM fluxes are compared with the EPT fluxes in a 2D-histogram in the years (a) 2016, (b) 2017 and (c) 2018. The correlation factors are (a) 0.83, (b) 0.82 and (c) 0.86. The magenta lines mark the deviation of one order of magnitude from the unity line.

## References


( ). Belgian Institute for Space Aeronomy - Space Environment Information System (SPENVIS). https://www.spenvis.oma.be/. Ver. 4.6.9, Last Accessed 13 May 2022.

( ). ESA Mission overview. URL: https://www.esa.int/Enabling_Support/Space_Engineering_Technology/Proba_Missions/Proba-V_carrying_radiation_detector_from_CERN_to_space. Last Accessed 13 May 2022.

Adams, J., Falconer, D., Fry, D., 2012. The Ionizing Radiation Environment in Space and Its Effects. In: Hu, Q., Li, G., Zank, G., Ao, X., Verkhoglyadova, O., Adams, J. (Eds.), Space Weather: The Space Radiation Environment, pp. 198–203. Univ Alabama, Ctr Space Plasma & Aeronom Res volume 1500 of AIP Conference Proceedings. 2012, https://doi.org/10.1063/1.4768766. 11th Annual International Astrophysics Conference (AIAC), Palm Springs, CA, MAR 19-23.

Agostinelli, S., Allison, J., Amako, K., et al., 2003. Geant4—a simulation toolkit. Nucl. Instrum. Methods Phys. Res. 506 (3), 250–303. https://doi.org/10.1016/S0168-9002(03)01368-8.

Baca, T., Jilek, M., Vertat, I., et al., 2018. Timepix in LEO Orbit onboard the VZLUSAT-1 nanosatellite: 1-year of space radiation dosimetry measurements. J. Inst. 13 (11), C11010. https://doi.org/10.1088/1748-0221/13/11/C11010.

Baker, D.N., Li, X., Turner, N., et al., 1997. Recurrent geomagnetic storms and relativistic electron enhancements in the outer magnetosphere: ISTP coordinated measurements. J. Geophys. Res. 102 (A7), 14141–14148. https://doi.org/10.1029/97JA00565.

Ballabriga, R., Alozy, J., Blaj, G., et al., 2013. The Medipix3RX: a high resolution, zero dead-time pixel detector readout chip allowing spectroscopic imaging. J. Instrum. 8 (02). https://doi.org/10.1088/1748-0221/8/02/c02016, C02016–C02016.

Ballabriga, R., Campbell, M., Llopart, X., 2020. An introduction to the Medipix family ASICs. Radiat. Meas. 136, 106271. https://doi.org/10.1016/j.radmeas.2020.106271.

Bergmann, B., Acharya, B., Alexandre, J. et al., MOEDAL Collaboration, 2021. Timepix3 as solid-state time-projection chamber in particle and nuclear physics. PoS, ICHEP2020, 720. 8 p. https://doi.org/10.22323/1.390.0720.

Bergmann, B., Billoud, T., Burian, P., et al., 2020. Relative luminosity measurement with Timepix3 in ATLAS. J. Instrum. 15 (01), C01039. https://doi.org/10.1088/1748-0221/15/01/C01039.

Bergmann, B., Billoud, T., Leroy, C., et al., 2019a. Characterization of the radiation field in the ATLAS experiment with timepix detectors. IEEE Trans. Nucl. Sci. 66 (7), 1861–1869. https://doi.org/10.1109/TNS.2019.2918365.

Bergmann, B., Burian, P., Manek, P., et al., 2019b. 3D reconstruction of particle tracks in a 2 mm thick CdTe hybrid pixel detector. Eur. Phys. J. C 79 (2), 165. https://doi.org/10.1140/epjc/s10052-019-6673-z.

Bergmann, B., Caicedo, I., Leroy, C., et al., 2016. ATLAS-TPX: a two-layer pixel detector setup for neutron detection and radiation field characterization. J. Instrum. 11 (10). https://doi.org/10.1088/1748-0221/11/10/p10002, P10002–P10002.

Bergmann, B., Pichotka, M., Pospisil, S., et al., 2017. 3D track reconstruction capability of a silicon hybrid active pixel detector. Eur. Phys. J. C 77 (6), 421. https://doi.org/10.1140/epjc/s10052-017-4993-4.

Boscher, D., Bourdarie, S.A., Falguere, D., et al., 2011. In Flight measurements of radiation environment on board the French Satellite JASON-2. IEEE Trans. Nucl. Sci. 58 (3), 916–922. https://doi.org/10.1109/TNS.2011.2106513.

Boscher, D., Cayton, T., Maget, V., et al., 2014. In-flight measurements of radiation environment on board the Argentinean Satellite SAC-D. IEEE Trans. Nucl. Sci. 61 (6), 3395–3400. https://doi.org/10.1109/TNS.2014.2365212.

Boteler, D., Pirjola, R., Nevanlinna, H., 1998. The effects of geomagnetic disturbances on electrical systems at the Earth's surface. Adv. Space Res. 22 (1), 17–27. https://doi.org/10.1016/S0273-1177(97)01096-X.

Butler, A., Anderson, N., Tipples, R., et al., 2008. Bio-medical X-ray imaging with spectroscopic pixel detectors. Nucl. Instrum. Methods Phys. Res. A 591 (1), 141–146. https://doi.org/10.1016/j.nima.2008.03.039, Radiation Imaging Detectors.

Cao, X., 2022. Research progress on the effects of microgravity and space radiation on astronauts' health and nursing measures. Open Astron. 31 (1), 300–309. https://doi.org/10.1515/astro-2022-0038.

Cyamukungu, M., Benck, S., Borisov, S., et al., 2014. The Energetic Particle Telescope (EPT) on Board PROBA-V: Description of a new science-class instrument for particle detection in space. IEEE Trans. Nucl. Sci. 61 (6), 3667–3681. https://doi.org/10.1109/TNS.2014.2361955.

Daglis, I.A., Thorne, R.M., Baumjohann, W., et al., 1999. The terrestrial ring current: origin, formation, and decay. Rev. Geophys. 37 (4), 407–438. https://doi.org/10.1029/1999RG900009.

Dudnik, O., Sylwester, J., Kowalinski, M., et al., 2022. Detection of the third innermost radiation belt on LEO CORONAS-Photon satellite around 2009 solar minimum. Adv. Space Res. 70 (5), 1441–1452. https://doi.org/10.1016/j.asr.2022.06.031.

Dungey, J.W., 1961. Interplanetary magnetic field and the auroral zones. Phys. Rev. Lett. 6, 47–48. https://doi.org/10.1103/PhysRevLett.6.47.

Evans, H., Bühler, P., Hajdas, W., et al., 2008. Results from the ESA SREM monitors and comparison with existing radiation belt models. Adv. Space Res. 42 (9), 1527–1537. https://doi.org/10.1016/j.asr.2008.03.022.

Fok, M.-C., Wolf, R.A., Spiro, R.W., et al., 2001. Comprehensive computational model of Earth's ring current. J. Geophys. Res. 106 (A5), 8417–8424. https://doi.org/10.1029/2000JA000235.

Francois, M., Santandrea, S., Mellab, K., et al., 2014. The PROBA-V mission: the space segment. Int. J. Remote Sens. 35 (7), 2548–2564. https://doi.org/10.1080/01431161.2014.883098.

Furnell, W., Shenoy, A., Fox, E., et al., 2019. First results from the LUCID-Timepix spacecraft payload onboard the TechDemoSat-1 satellite in Low Earth Orbit. Adv. Space Res. 63 (5), 1523–1540. https://doi.org/10.1016/j.asr.2018.10.045.

Gohl, S., Bergmann, B., Evans, H., et al., 2019. Study of the radiation fields in LEO with the Space Application of Timepix Radiation Monitor (SATRAM). Adv. Space Res. 63 (5), 1646–1660. https://doi.org/10.1016/j.asr.2018.11.016.

Gohl, S., Malich, M., Bergmann, B., et al., 2022. A miniaturized radiation monitor for continuous dosimetry and particle identification in space. J. Instrum. 17 (01), C01066. https://doi.org/10.1088/1748-0221/17/01/c01066.

Gonzalez, W.D., Joselyn, J.A., Kamide, Y., et al., 1994. What Is a Geomagnetic Storm? J. Geophys. Res. 99 (A4), 5771–5792. https://doi.org/10.1029/93JA02867.

Granja, C., Polansky, S., Vykydal, Z., et al., 2016. The SATRAM Timepix spacecraft payload in open space on board the PROBA-V satellite for wide range radiation monitoring in LEO orbit. Planet. Space Sci. 125, 114–129. https://doi.org/10.1016/j.pss.2016.03.009.

Holy, T., Heijne, E., Jakubek, J., et al., 2008. Pattern recognition of tracks induced by individual quanta of ionizing radiation in Medipix2 silicon detector. Nucl. Instrum. Methods Phys. Res. 591 (1), 287–290. https://doi.org/10.1016/j.nima.2008.03.074, Radiation Imaging Detectors.

Jakubek, J., 2011. Precise energy calibration of pixel detector working in time-over-threshold mode. Nucl. Instrum. Methods Phys. Res. 633, S262–S266. https://doi.org/10.1016/j.nima.2010.06.183, 11th International Workshop on Radiation Imaging Detectors (IWORID).

Jordanova, V.K., Kozyra, J.U., Nagy, A.F., et al., 1997. Kinetic model of the ring current-atmosphere interactions. J. Geophys. Res. 102 (A7), 14279–14291. https://doi.org/10.1029/96JA03699.

Kappenman, J.G., 1999. Geomagnetic storm and power system impacts: advanced storm forecasting for transmission system operations. In: 1999 IEEE Power Engineering Society Summer Meeting. Conference Proceedings (Cat. No. 99CH36364), vol. 2, IEEE, pp. 1187–1191.

Kikuchi, T., 2003. Space weather hazards to communication satellites and the space weather forecast system. In: In 21st International Communications Satellite Systems Conference and Exhibit, p. (p. 2254).. https://doi.org/10.2514/6.2003-2254.

Kovtyukh, A.S., 2020. Earth's radiation belts' ions: patterns of the spatial-energy structure and its solar-cyclic variations. Ann. Geophys. 38 (1), 137–147. https://doi.org/10.5194/angeo-38-137-2020.

Kroupa, M., Bahadori, A., Campbell-Ricketts, T., et al., 2015. A semiconductor radiation imaging pixel detector for space radiation dosimetry. Life Sci. Space Res. 6, 69–78. https://doi.org/10.1016/j.lssr.2015.06.006.

Llopart, X., Ballabriga, R., Campbell, M., et al., 2007. Timepix, a 65k programmable pixel readout chip for arrival time, energy and/or photon counting measurements. Nucl. Instrum. Methods Phys. Res. 581 (1), 485–494. https://doi.org/10.1016/j.nima.2007.08.079, VCI.

Maget, V., Bourdarie, S., Lazaro, D., et al., 2014. Unfolding JASON-2/ICARE-NG High-energy particles measurements using a singular value decomposition approach. IEEE Trans. Nucl. Sci. 61 (4), 1687–1694. https://doi.org/10.1109/TNS.2014.2300161.

Pandya, M., Bhaskara, V., Ebihara, Y., et al., 2019. Variation of radiation belt electron flux during CME- and CIR-driven geomagnetic storms: Van Allen Probes Observations. J. Geophys. Res. 124 (8), 6524–6540. https://doi.org/10.1029/2019JA026771.

Pierrard, V., Botek, E., Ripoll, J.-F., et al., 2020. Electron dropout events and flux enhancements associated with geomagnetic storms observed by PROBA-V/energetic particle telescope. J. Geophys. Res. 125 (12). https://doi.org/10.1029/2020JA028487, e2020JA028487. from 2013 to 2019.

Pierrard, V., Ripoll, J.-F., Cunningham, G., et al., 2021. Observations and simulations of dropout events and flux decays in October 2013: Comparing MEO equatorial with LEO Polar Orbit. J. Geophys. Res. 126 (6). https://doi.org/10.1029/2020JA028850, e2020JA028850.

Poikela, T., Plosila, J., Westerlund, T., et al., 2014. Timepix3: a 65K channel hybrid pixel readout chip with simultaneous ToA/ToT and sparse readout. J. Instrum. 9 (05). https://doi.org/10.1088/1748-0221/9/05/c05013, C05013–C05013.

Procz, S., Avila, C., Fey, J., et al., 2019. X-ray and gamma imaging with Medipix and Timepix detectors in medical research. Radiat. Meas. 127, 106104. https://doi.org/10.1016/j.radmeas.2019.04.007.

Rosenfeld, A., Alnaghy, S., Petasecca, M., et al., 2020. Medipix detectors in radiation therapy for advanced quality-assurance. Radiat. Meas. 130, 106211. https://doi.org/10.1016/j.radmeas.2019.106211.

Ruffenach, M., Bourdarie, S., Bergmann, B., et al., 2021. A new technique based on convolutional neural networks to measure the energy of protons and electrons with a single timepix detector. IEEE Trans. Nucl. Sci. 68 (8), 1746–1753. https://doi.org/10.1109/TNS.2021.3071583.

Sandberg, I., Daglis, I.A., Anastasiadis, A., et al., 2011. Unfolding and validation of srem fluxes. In: 2011 12th European Conference on Radiation and Its Effects on Components and Systems, pp. 599–606. https://doi.org/10.1109/RADECS.2011.6131429.

Sawyer, D.M., Vette, J.I., 1976. Trapped Particle Environment for Solar Maximum and Solar Minimum (AP8). Technical Report NSSDC Report 76-06.

Siegl, M., Evans, H.D.R., Daly, E.J., et al., 2010. Inner belt anisotropy investigations based on the standard radiation environment monitor (SREM). IEEE Trans. Nucl. Sci. 57 (4), 2017–2023. https://doi.org/10.1109/TNS.2010.2041253.

Stoffle, N., Pinsky, L., Kroupa, M., et al., 2015. Timepix-based radiation environment monitor measurements aboard the International Space Station. Nucl. Instrum. Methods Phys. Res. 782, 143–148. https://doi.org/10.1016/j.nima.2015.02.016.

Sugiura, M., 1964. Hourly Values of Equatorial Dst For the IGY. Ann. Int. Geophys. Yr., 35.

Tichy, V., Holy, T., Jakubek, J., et al., 2008. X-ray fluorescence imaging with pixel detectors. Nucl. Instrum. Methods Phys. Res. 591 (1), 67–70. 2007. https://doi.org/10.1016/j.nima.2008.03.122, Radiation Imaging Detectors.

Tripathi, R.K., 2011. Radiation Effects In Space. In: McDaniel, F.D., Doyle, B.L. (Eds.), Application Of Accelerators In Research And Industry: Twenty-First International Conference, pp. 649–654. Univ N Texas; Sandia Natl Labs; Los Alamos Natl Lab; AccSys Technol Inc; High Voltage Engn Europa BV; Natl Electrostat Corp; TDK-Lambda Amer volume 1336 of AIP Conference Proceedings. doi:10.1063/1.3586182 21st International Conference on Application of Accelerators in Research and Industry (CAARI), Ft Worth, TX, AUG 08-13, 2010.

Turner, D.L., Kilpua, E.K.J., Hietala, H., et al., 2019. The response of Earth's electron radiation belts to geomagnetic storms: statistics from the Van Allen Probes Era Including effects from different storm drivers. J. Geophys. Res. 124 (2), 1013–1034. https://doi.org/10.1029/2018JA026066.

Vette, J., 1991. The AE-8 trapped electron model environment. Technical Report NSSDC/WDC-A-RS-91-24.

Walt, M., 1996. Source and loss processes for radiation belt particles. In: Radiation Belts: Models and Standards. American Geophysical Union (AGU), pp. 1–13. https://doi.org/10.1029/GM097p0001.

Wong, W., Alozy, J., Ballabriga, R., et al., 2020. Introducing Timepix2, a frame-based pixel detector readout ASIC measuring energy deposition and arrival time. Radiat. Meas. 131, 106230. https://doi.org/10.1016/j.radmeas.2019.106230.

Zhao, H., Baker, D.N., Li, X., et al., 2019. The effects of geomagnetic storms and solar wind conditions on the ultrarelativistic electron flux enhancements. J. Geophys. Res. 124 (3), 1948–1965. https://doi.org/10.1029/2018JA026257.

Žemlicka, J., Jakubek, J., Kroupa, M., et al., 2009. Energy- and position-sensitive pixel detector Timepix for X-ray fluorescence imaging. Nucl. Instrum. Methods Phys. Res. 607 (1), 202–204. 2008. https://doi.org/10.1016/j.nima.2009.03.140.